Damage accumulation and hysteretic behavior of MAX phase materials

B. Poon, L. Ponson*, J. Zhao, G. Ravichandran

Graduate Aerospace Laboratories, California Institute of Technology, Pasadena, CA 91125, USA

ARTICLE INFO

ABSTRACT

The compressive response of fully dense and 10 vol% porous Ti_2AlC MAX phase materials subjected to quasi-static uniaxial and cyclic loading including their repeatable hysteretic behavior is presented. Damage accumulation in the form of kink bands and microcracking is characterized using ultrasonics and scanning electron microscopy under different levels of compressive loading. The observations and measurements are correlated quantitatively using a model based on friction between the crack faces, which is the main dissipation process. The model is shown to capture the hysteretic behavior of Ti_2AlC MAX phase and quantitatively reproduce the experimentally measured stress–strain curves.

© 2011 Elsevier Ltd. All rights reserved.

1. Introduction

The MAX phases, with the chemical composition $M_{n+1}AX_n$, where $n \in \{1,2,3\}$, M is an early transition metal, A is a A-group element (mostly IIIA and IVA) and X is C or N. MAX phases have received considerable attention in the recent years for their unique properties, namely soft, machinable, thermally and electrically conductive like a metal, yet heat tolerant, light and strong like a ceramic (Barsoum and El-Raghy, 2001; Barsoum et al., 2003; Sun et al., 2005; Zhen et al., 2005; Zhou et al., 2006). This family of materials has considerable potential in many novel applications (Barsoum and El-Raghy, 2001).

Ti_2AlC is a particular member of the family of MAX phases with all their outstanding material properties (Barsoum et al., 1997, 2000, 2002; Wang and Zhou, 2003; Zhou et al., 2006). Considering Ti_2AlC as a candidate material for structural applications, its mechanical behavior, both under quasi-static and dynamic loading, have to be well described and understood. The first study devoted to its quasi-static behavior has been reported (Zhou et al., 2006), where uniaxial compression and spherical nano-indentation tests were conducted. Ti_2AlC was observed to possess qualities similar to the other MAX phases characterized in particular by a repeatable hysteretic behavior under cyclic loading. These results were interpreted using a model developed recently to account for the behavior of a broader family of materials with similar mechanical properties and referred to as kinking nonlinear elastic (KNE) solids (Barsoum et al., 2005; Kalidnindi et al., 2006). In this approach, the formation and evolution at the atomic scale of dislocation-based kink bands is proposed to explain such reversible hysteresis behavior. Though this theoretical description explains the main qualitative features of the macroscopic response of MAX phases (reversibility, hysteresis), it cannot capture their constitutive behavior. Continuum damage mechanics (CDM) description based on microstructural observations provides an avenue for developing a model to capture the quantitative response of this new class of materials.

---

* Corresponding author. Present address: Institut d'Alembert, CNRS - UPMC, Paris. Tel.: +1 626 395 4178; fax: +1 626 568 2719.
  E-mail address: ponson@caltech.edu (L. Ponson).

The present paper addresses the compressive response of fully dense and 10 vol% porous Ti_2AlC subjected to quasi-static uniaxial and cyclic loading. Careful strain measurements in both axial and transverse directions were carried out to fully characterize the repeatable hysteretic behavior of Ti_2AlC. New features suggesting the formation and evolution of damage processes during the tests are reported. These results are combined with post-mortem ultrasonic measurements aimed at assessing the extent of damage accumulation during the experiments. Scanning electron microscopy (SEM) characterization of the MAX phase under different levels of compressive loading is also used to observe directly the damage processes and their evolution. The ultrasonic technique reveals a weak degradation of both Young's modulus and Poisson's ratio during the compressive test that is likely produced by the formation of kink bands observed in the SEM micrographs. The SEM characterization allows one to identify the presence of a large number of delamination cracks within the MAX phase grains. The crack density is measured and shown to increase with the external loading, suggesting that these cracks might be responsible for the hysteretic behavior of Ti_2AlC observed also to be more pronounced with increasing compressive loading. Both these observations are related more quantitatively using a theoretical description of the experiments inspired by Walsh (1965) and Lawn and Marshall (1998) in which friction between the delamination crack faces is the main dissipation process during the compressive test. This simple model, based only on the observable damage mechanisms, not only mimics the hysteretic behavior of Ti_2AlC, but also reproduces quantitatively the experimental stress–strain curves. To check the consistency of the model, the crack density used in the model is compared with that obtained directly from SEM images, showing a good agreement between the two.

2. Materials and methods

The uniaxial compressive tests under quasi-static loading were conducted using a servo-hydraulic Materials Testing System (MTS 358 series) under displacement control at a nominal strain rate ranging from 10^{-5} to 10^{-3} s^{-1}. Rectangular blocks of Ti_2AlC ($7 \times 7 \times 17$ mm^3) were made using wire electro-discharge machining (EDM). Special attention was given to the surface finish and extent of parallelism between the two loaded surfaces (7×7 mm^2 faces), with a tolerance of 0.02 mm. Strain measurements were made using 350 Ω strain gages (Vishay, EA-06-062AQ-350/LE) that were attached to the sides of the specimen along directions parallel and perpendicular to the loading axis.

The effect of the uniaxial compressive loading on Young's modulus and Poisson's ratio of Ti_2AlC were investigated using ultrasonic wave speed measurements performed on the specimens after they were unloaded. The longitudinal and shear wave speeds were measured using 5 MHz piezoelectric longitudinal and shear transducers (#V129 and #V157, Parametrics, Inc.), in pulse-echo mode setup. The pulse was generated using Parametrics Pulse Generator model #5052A, with a peak output voltage of 300 V. The signals were acquired using a Hewlett Packard digitizing oscilloscope model #50510A, with a sampling rate of 1 GSa s^{-1}.

Finally, Ti_2AlC specimens submitted to different levels of compressive loading were mounted and polished to mirror finish for microstructural characterization. The specimens were then slightly etched using a solution of hydrofluoric acid, nitric acid and water in equal amounts to reveal the microstructure. Scanning electron microscopic observations were performed on these specimens as well as on the fracture surfaces of broken specimens using a LEO 1550VP FE SEM.

3. Results

3.1. Stress–strain behavior

The typical stress–strain behavior of Ti_2AlC under compression is shown in Fig. 1(a) and (b) for dense and porous samples, respectively. The specimens were incrementally loaded and unloaded to failure as evidenced by the final cycle. During the last cycle, the stress increases almost monotonically until abrupt failure of the specimen. The solid and dashed lines represent the loading–unloading cycles performed on a single specimen. The first cycle begins at the origin, and each subsequent cycle begins at the residual strain left from the previous one. By connecting the part of each loop prior to unloading, one obtains the strain–strain curve of a specimen that is loaded monotonically to failure. This curve is well described by a power-law relationship between stress and strain, classically used to describe the effects of plasticity and damage in quasi-brittle systems before abrupt failure. The unloading curve shows irreversibility with a compressive residual strain when compressive loading is zero. This macroscopic nonlinear behavior will be related in the next section with microscopic mechanisms such as irreversible damage accumulation during the loading phase of the specimen. These experiments were observed to be highly repeatable. Such incremental tests were not reported in the previous study (Zhou et al., 2006), and they provide the information to be used for the characterization of damage accumulation in this material.

In the experiments presented in Fig. 1, specimens of dense and porous specimens have been submitted to cycles with increasing maximum strain until full failure obtained around 0.91 and 0.48 GPa, respectively. Young's modulus for dense and 10 vol% porous Ti_2AlC measured from the linear part of stress–strain curves is found to be approximately 250 and 205 GPa, respectively. Poisson's ratio of dense and porous Ti_2AlC obtained from the measurement of the transverse strain during the uniaxial compression (Fig. 2) is found to be approximately 0.17 and 0.3, respectively. For sake of simplicity, we have expressed the compressive axial stress and strain as positive quantities.
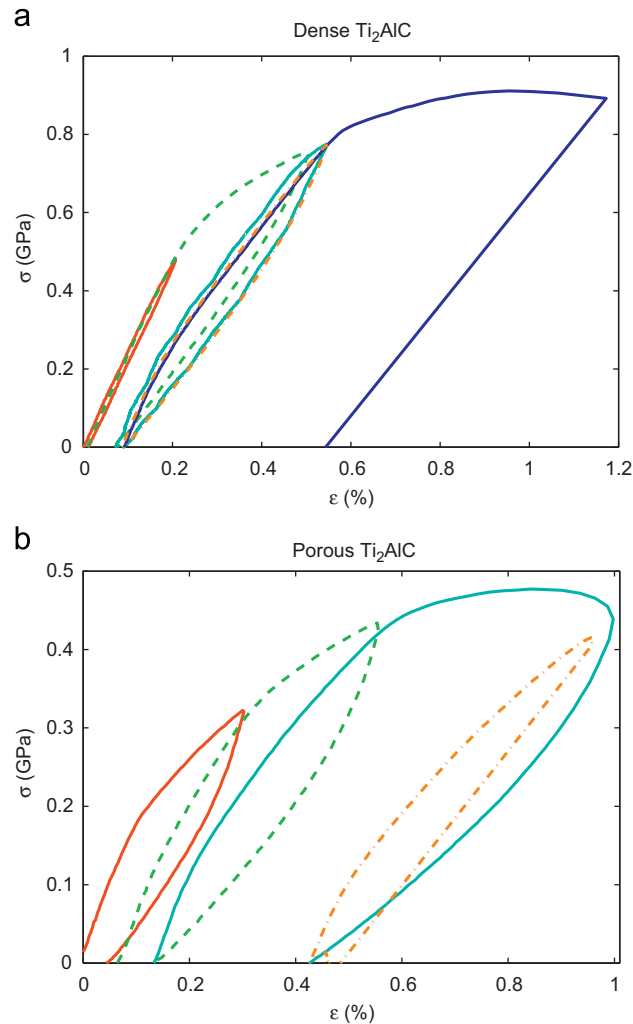
Fig. 1. Stress–strain curves for (a) dense and (b) porous Ti$_2$AlC, under repeated compressive loading.

From Fig. 1, a yield point can be distinctly identified for both dense and porous Ti$_2$AlC. Dense Ti$_2$AlC is observed to yield at approximately 0.54 GPa, whereas porous Ti$_2$AlC yields at approximately 0.13 GPa. In the initial linear regime, the loading and unloading part of the stress–strain curves coincides for both the dense and porous Ti$_2$AlC, as expected for a linearly elastic material. Beyond the yield point, hysteresis loops are observed, similar to those described in Barsoum and El-Raghy (2001), Zhen et al. (2005) and Zhou et al. (2006). These cycles are highly repeatable and independent of the strain rates at which the specimen was loaded within the range of strain rates considered here. The unloading and reloading curves differ when the accumulated strain is beyond the yield point and also there is residual strain upon unloading whose magnitudes increases with increasing applied strain.

These observations suggest that while the virgin material is initially linearly elastic, damage is accumulated beyond yield and the stress–strain behavior is no longer linear. The occurrence of hysteresis loops points to damage accumulation beyond yield.

The failure stress of the dense Ti$_2$AlC is approximately 0.89 GPa while the porous ceramics breaks around 0.44 GPa. The corresponding strain at failure is approximately 1.2% and 1.0%, respectively. As shown in Fig. 3, the fracture plane is oriented at 45° with respect to the axis of loading, suggesting that Ti$_2$AlC fails by a shear mechanism. As described in detail in the following, catastrophic failure can be entailed to the nucleation and growth of microcracks in the specimen that coalesce and form a macroscopic shear crack just prior failure.

3.2. Stress–strain behavior under cyclic loading

In order to study in detail the behavior of Ti$_2$AlC under cyclic loading, a dense and a porous specimen were submitted to 100 cycles at a frequency of 0.5 Hz. Their mechanical response is plotted in Fig. 4. For both samples and beyond the first cycle, the hysteresis loop is almost stabilized. A slight cyclic hardening can be observed for both the fully dense and the porous specimen, with somehow slightly larger amplitude for the dense ceramics. These results confirm and extend the
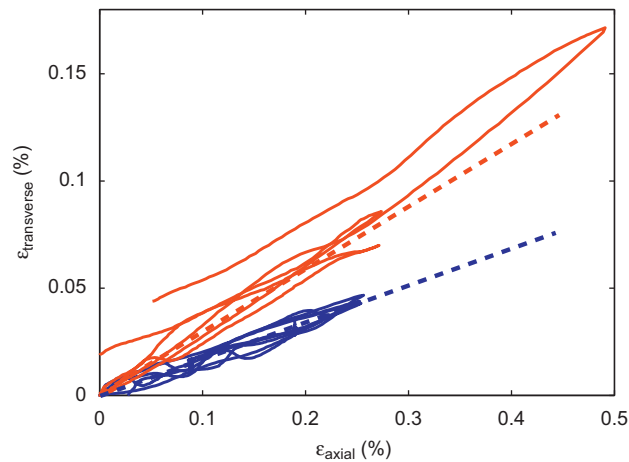
Fig. 2. Axial strain versus transverse strain for dense (blue) and porous (red) Ti$_2$AlC. The dashed lines are the trend lines of the initial elastic response. Let us note here that ε_{axial} and $\varepsilon_{transverse}$ are compressive and tensile strains, respectively, that we noted both positively by convention. (For interpretation of the references to color in this figure legend, the reader is referred to the web version of this article.)
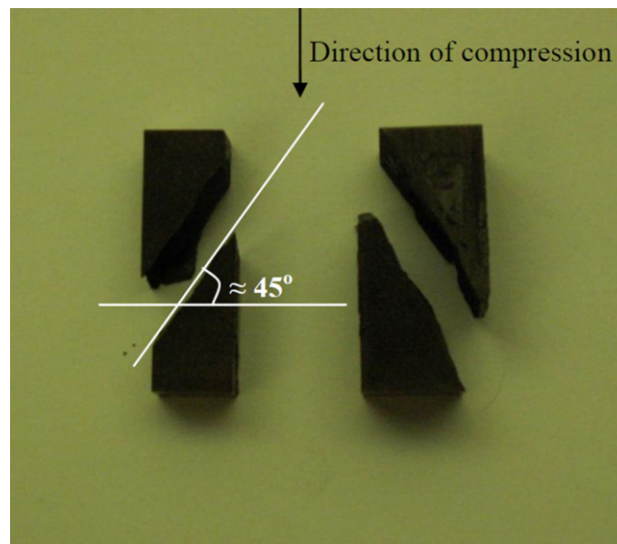
Fig. 3. Fractured Ti$_2$AlC specimens under uniaxial compressive loading. Note the fracture plane at 45° with respect to the direction of loading.

experimental results reported by Zhou et al. (2006) on the same material submitted to 3–5 cycles to a large number of cycles. The microscopic origin of this effect is discussed in Section 4.

3.3. Effects of strain rate and relaxation

In order to investigate the effect of strain rate and the presence of visco-elastic relaxation in dense and porous Ti$_2$AlC, two different experiments have been conducted. In the first experiment, uniaxial compressions were carried out at different strain rates, ranging from 10^{-5} to 10^{-3} s^{-1}. No strain rate effects were observed on the recorded stress–strain curves. In another experiment, the specimens were loaded sequentially under displacement control, as shown in Fig. 5(a). Between rest phases, the displacement was imposed at the same strain rate all along the experiment. The corresponding stress–strain curves plotted in Fig. 5(b) do not show any noticeable effect, suggesting that both dense and porous Ti$_2$AlC do not exhibit any stress relaxation or visco-elastic response.

3.4. Effects of the compressive loading on Young's modulus and Poisson's ratio

Ultrasonic wave speed measurements were used to investigate changes in the Ti$_2$AlC microstructure induced by the compressive loading of various levels. In this series of experiments, only the dense specimens were considered since wave speed measurements in porous specimens were difficult due to significant wave scattering by the voids.
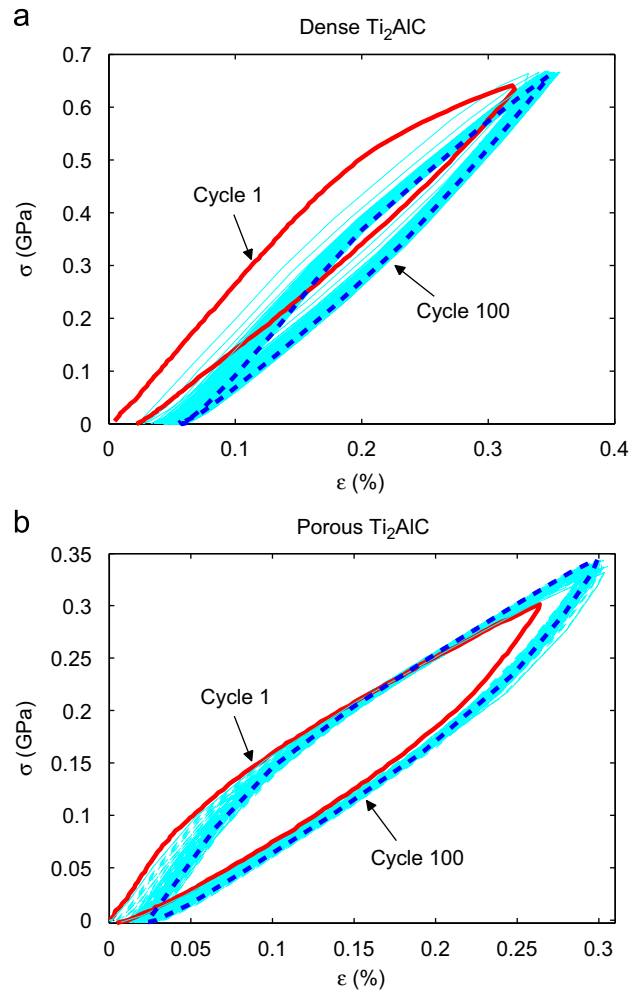
Fig. 4. Stress–strain curves for cyclically loaded (a) dense and (b) porous Ti$_2$AlC.

Four dense Ti$_2$AlC specimens were compressed to different strain levels (0.15%, 0.19%, 0.4% and 0.76%) and the corresponding stress–strain curves are shown in Fig. 6. We extracted Young's modulus of each specimen by a linear fit of the data in the unloading part, just after the maximum stress has been reached, and found values of 250, 245, 235 and 213 GPa, respectively. This part of the stress–strain response is governed by the elastic response of the damaged specimen, as we will show in Section 4 (see also Fig. 13 for more details on the fit procedure). As a result, one can compare these values with elastic properties obtained by acoustic techniques: the longitudinal and shear wave speeds were measured after the experiments and their values are shown in Table 1. The waves propagated along a direction perpendicular to the symmetry axis of the cylindrical specimens, and hence perpendicular to the direction of the compression loading. As a result, Young's modulus extracted from the mechanical test and the acoustic measurements corresponds to two perpendicular directions. From the acoustic measurements, we see a small, however, a clear trend that indicates that the wave speed is lower for specimens submitted to higher strains, which accumulated more damage. In order to estimate the relevance of this observation, let us assess the accuracy of the measurement: we consider a typical precision of 10 µm for the length and 1 ns for the time measurements. For a typical specimen thickness of 7 mm and measurement duration of 1 µs, the uncertainty for velocity measurement is of the order of 0.14%. This value is smaller than the measured differences in wave velocities of the 4 specimens, indicating that, although small, the trend is significant.

The decrease of the longitudinal V_l and shear wave speeds V_s corresponds to changes in Young's modulus E and Poisson's ratio v. These quantities for a linear elastic solid are related by the relations $v = (1/2 - (V_s/V_l)^2)/(1/2 + (V_s/V_l)^2)$ and $E = 2\rho_s V_s^2(1+v)$ where $\rho_s = 3950$ kg m^{-3} is the density of Ti$_2$AlC. The elastic properties measured from this technique are represented in Fig. 7 for different levels of external strain. At first, the value of E and v are comparable with the value $E_0 = 250$ GPa and $v_0 = 0.17$ extracted from the stress–strain behavior of Ti$_2$AlC in the elastic domain (see Figs. 1 and 2). It also compares with the values obtained from the stress–strain response in the unloading part of the cycle (see Fig. 6). Investigating now the effect of the compressive loading, one observes a slight decrease of Young's modulus obtained both from the acoustic measurement and the mechanical test. This seems to correspond to a steady degradation of the stiffness
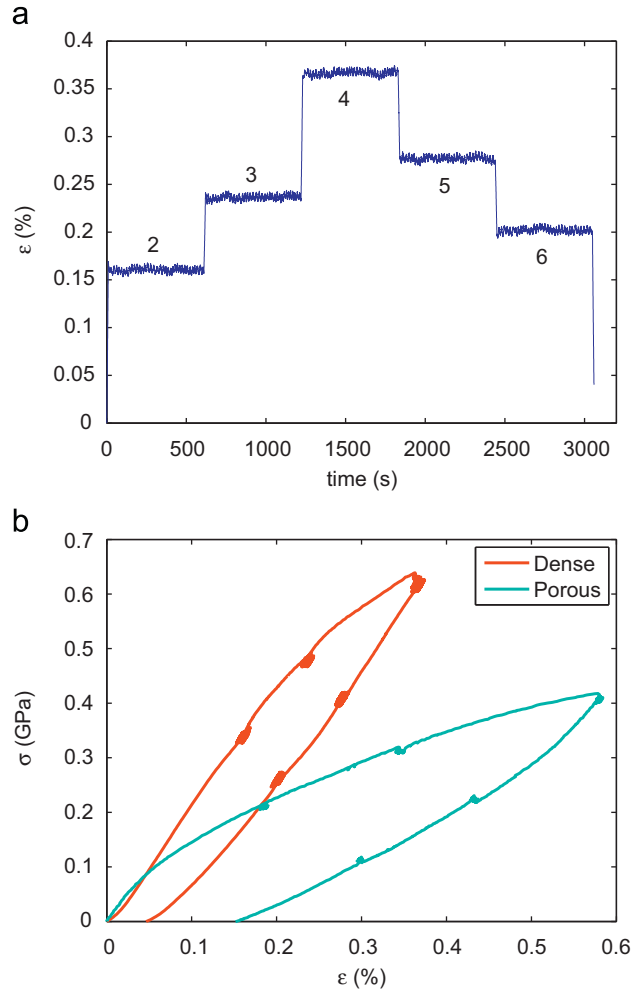
Fig. 5. Investigation of visco-elastic effects and stress relaxation in MAX ceramics: (a) strain applied to the dense specimen as a function of time, (b) corresponding stress–strain curve for dense (red) and porous (blue) Ti$_2$AlC. (For interpretation of the references to color in this figure legend, the reader is referred to the web version of this article.)
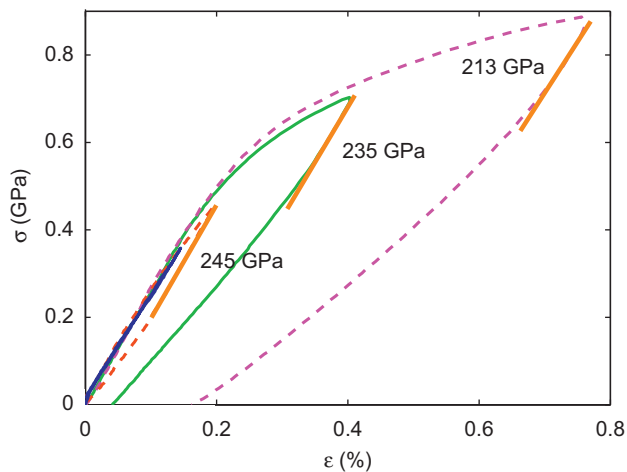

Fig. 6. Four fully dense Ti$_2$AlC specimens loaded in compression to strain levels of 0.15%, 0.19%, 0.4% and 0.76%. Young's moduli at various development of the damage in the specimen are extracted by fitting the linear part of the unloading curve just next to the maximum applied strain as represented by the straight solid lines (see Section 4 for justification).

Table 1
Longitudinal and shear wave speeds measured on the specimens submitted to different levels of strain once unloaded.

ε_{max} (%)	V_l (km s^{-1})	V_s (km s^{-1})
0.15	8.385	5.137
0.19	8.313	5.111
0.4	8.321	5.159
0.76	8.143	5.088
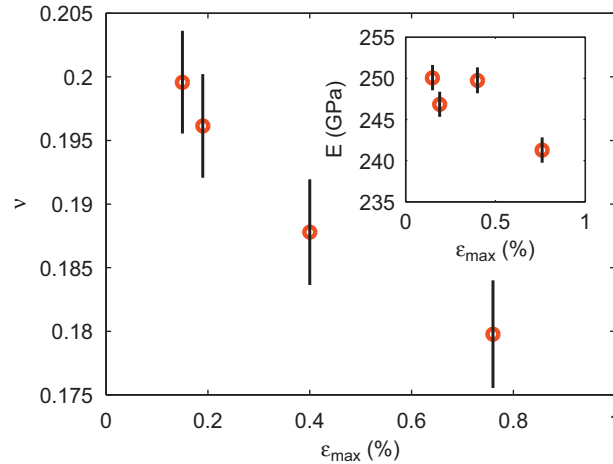
Fig. 7. Variations of Poisson's ratio (main panel) and Young's modulus (inset) with the maximum applied strain as computed from ultrasonic measurements.

of the specimen as damage develops within the ceramics, somehow less important when extracted from the acoustic technique. This effect might be explained by some anisotropy in the elastic properties of the solid resulting from the development of damage in a preferential direction given by the loading axis—mechanic and acoustic measurements provide information parallel and perpendicular to the loading axis, respectively. The variations of Poisson's ratio are shown in the main panel of Fig. 7. One observes also a rather significant decrease of ν with the level of applied strain. Both trends strongly suggest an evolution of the Ti$_2$AlC microstructure during the test. Damage produced by the high level of compression in the specimen is likely to produce such alteration in the elastic properties of Ti$_2$AlC. These suggested damage processes are studied in more detail in the following section using direct observations of the microstructure of Ti$_2$AlC on the fracture surfaces of broken specimens.

3.5. Fractographic analysis

The fracture surfaces of the dense Ti$_2$AlC specimens were examined using the SEM. Fig. 8 shows the macroscopic fracture surface, with the direction of crack propagation indicated. The lack of distinctive features at this low magnification does not point to a specific fracture mechanism. Upon larger magnification, as shown in Fig. 9, damage mechanisms such as kink bands, delamination cracks between the nanolayers, and inter-granular cracks are readily observed.

The fracture surfaces of the porous samples were observed under the SEM as well (Fig. 10). As expected, more voids are observed as compared to the dense specimens. Larger magnification (Fig. 11) reveals the same overall damage mechanisms, namely kink bands, delamination and inter-granular cracks. In the following, these observations are used to interpret the mechanical response of Ti$_2$AlC specimens under compressive loading.

4. Discussion

Ti$_2$AlC is a member of the MAX phases, which have been commonly modeled as kinking nonlinear elastic (KNE) solids (Barsoum et al., 2005; Kalidindi et al., 2006; Sun et al., 2005). The characteristics of KNE solids is that the hysteresis loop is fully reversible, and rate-independent. The model for KNE solids, discussed in detail by Sun et al. (2005), considers these reversible hysteresis loops as resulting from the reversible formation and annihilation of incipient kink bands (IKB) and dislocation pileups (DP). This microscale model, which builds on the Frank and Stroh (1952) model for kink bands formation, provides a good estimate of the dissipated energy (Sun et al., 2005), but not the actual stress–strain relationship. By combining this approach to the assumption that the probability of kinking is given by Weibull statistics,
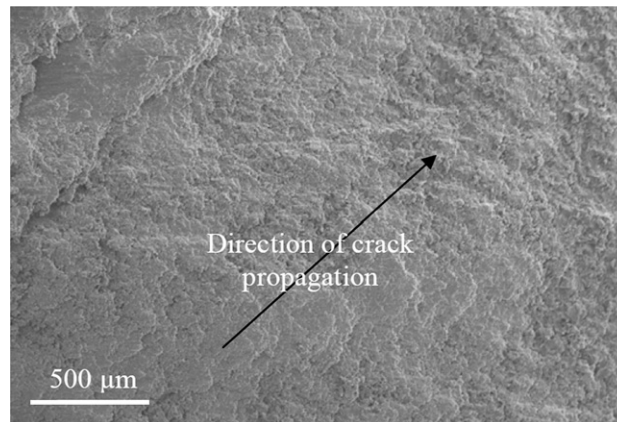
Fig. 8. Fracture surface of fully dense Ti$_2$AlC (low magnification).
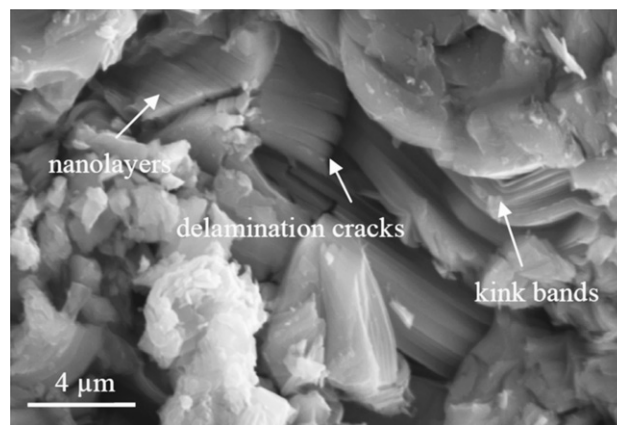
Fig. 9. Fracture surface of fully dense Ti$_2$AlC (high magnification).
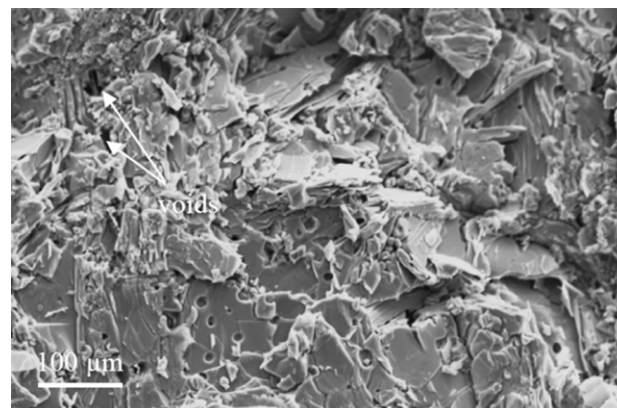
Fig.10. Fracture surface of porous Ti$_2$AlC (low magnification).

a macroscale constitutive model was presented (Kalidindi et al., 2006). The results derived from this model were then demonstrated to capture the general stress–strain behavior of KNE solids that is measured experimentally, though not quantitatively.

In the subsequent section, an alternative micromechanical model for the behavior of MAX phases is presented. Unlike the existing models for the MAX phases, the proposed model does not consider a reversible dislocation based mechanism. The proposed micromechanical model attempts to explain the features observed in the experimentally measured stress–strain
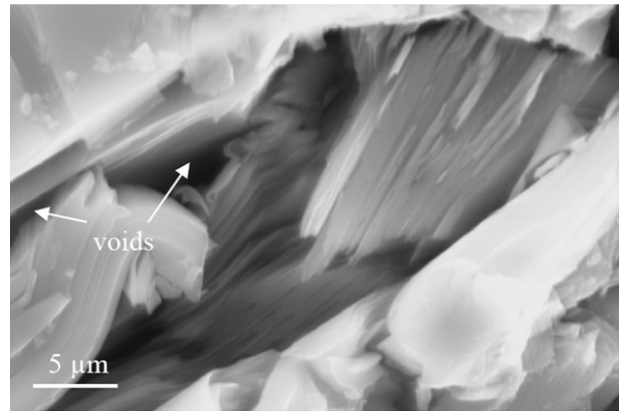
Fig. 11. Fracture surface of porous Ti_2AlC (high magnification).

curves using only the damage mechanisms observed in the SEM images. The interesting additional information derived from this model is of analysis of the estimation of the crack density in the material, which can and will be verified quantitatively using a statistical technique on the SEM images. While this study considers Ti_2AlC as the material of interest, it should be noted that this model can be used as a means of estimating the crack density in similar composites or brittle solids containing closed cracks.

4.1. Micromechanical model

The SEM pictures for preloaded Ti_2AlC reveal three types of damage mechanisms (i) kink bands, (ii) delamination cracks between nanolayers and (iii) inter-granular cracks. It is also rather clear from the uniaxial stress–strain behavior that damage accumulation begins when the stress exceeds the yield stress ($\sigma > \sigma_y$) since, as long as the latter is not exceeded, (i) there is no degradation of Young's modulus and (ii) there are no hysteresis loops and the specimen behaves like a linear elastic material. Two simplifying assumptions are made in this micromechanical model:

1. The degradation of Young's modulus is attributed to the kink bands.
2. The hysteresis of the stress–strain curve is attributed to the sliding of the cracks.

The first assumption can be justified as follows. The kink bands as observed in the SEM images resemble buckled nanolayers. Their contribution to the degradation of the elastic modulus E_o may be qualitatively understood on the basis that an unbuckled beam is stiffer than a buckled one. On the other hand, the cracks observed on the SEM images that develop in the specimens during the compression test remain closed during the experiments. These closed cracks do not contribute to the degradation of E_o measured by acoustic measurements. Indeed, the shearing forces imposed by the acoustic waves on crack surfaces are not sufficiently large to overcome their resistance to sliding induced by friction. It is worth noting that most of the kink bands will be oriented along the loading axis of the uniaxial compression leading to anisotropic degradations of the elastic properties of the specimens. This might explain why the change in Young's modulus assessed by acoustic measurements performed along a direction perpendicular to this axis is found to be relatively weak compared to the effective Young's modulus decrease measured along the loading direction from the stress–strain curves (see Section 3.4). On the other hand, Poisson's ratio degradation measured using acoustic techniques are significant because they correspond to deformations parallel to the loading axis along which most of kink bands are expected to be aligned.

The second assumption can also be justified by rather simple arguments. Once a kink band has buckled, additional loading and unloading will not give rise to a hysteretic behavior. One may also expect that their individual mechanical response remains mainly linear, if the compressive load is not increased further. Therefore, the response of the Ti_2AlC samples submitted repeatedly to a given compressive load cannot be explained by the presence of kink bands, and their effects on the nonlinear behavior of Ti_2AlC within one cycle can be neglected as a first approximation. We will show further that sliding of closed cracks can account for these nonlinearities, and the accompanying friction processes are responsible for energy dissipation in the system.

Finally, let us note that the accumulation of damage in the specimen during the test is made possible due to the material microstructure. Generally, for compressive tests without lateral confinement, the first shear crack transects the specimen leading to catastrophic failure without damage accumulation. But for the Ti_2AlC samples, as it will be clear later by investigating the material microstructure and the damage processes using SEM images, microcracks are stopped by grain boundaries, so they are confined to one single grain. This is also important to note that the shear cracks in Ti_2AlC samples do not kink to develop tensile cracks at their tip, as observed on the SEM images. This allows us to describe relatively simply the effect of microcracks on the overall mechanical response of the material.

As a result, the physical description for the micromechanical behavior under uniaxial compressive loading is expected to be as follows: as the virgin specimen is loaded, cracks and kink bands are created; upon unloading, the specimen is unloaded elastically until the resolved shear stress on the crack face overcomes the frictional threshold so that the crack faces then begin to slide relative to each other. As more cracks begin to slide, the effective modulus of the material becomes significantly smaller than its initial elastic Young's modulus, E_o. Upon reloading, the frictional force changes its direction, thus the material is loaded elastically before its resolved shear stress overcomes again the frictional threshold and sliding begins in the opposite direction. It is important to note that the elastic stiffness E_o of the material at any stage is dependent on the density of kink bands in the specimen. This results in the hysteresis loops observed in the experimental stress–strain data. The subsequent discussion in this section will focus on dense Ti$_2$AlC however a similar treatment can be applied to porous specimens as well.

The proposed model first considers randomly distributed cracks whose density is dependent on the maximum strain achieved by the specimen during prior loadings. The hysteresis in the unloading and reloading stress–strain curves is attributed to the frictional dissipation from the sliding of the closed cracks inside the material as previously proposed (Kachanov, 1982; Lawn and Marshall, 1998; Lehner and Kachanov, 1995; Walsh, 1965).

4.1.1. Friction law

In this model, the frictional stress, τ_f, at the crack faces is modeled by Coulomb's friction law:

$$\tau_f = \mu\sigma\sin^2\beta, \tag{1}$$

where μ is the coefficient of friction, σ is the uniaxial compressive stress and β is the crack orientation as illustrated in Fig. 12. In the following, we will consider a random orientation of the embedded microcracks in the specimen.

4.1.2. General unloading and reloading stress–strain relationships

The general unloading and reloading stress–strain relationships is derived using the same approach as that employed by Kachanov (1982), Lawn and Marshall (1998), Lehner and Kachanov (1995) and Walsh (1965). The basis of the derivation considers the complementary energy density for the cracked body as a linear summation of the complementary energy density of a body without crack and the crack density energy, W. Considering non-interacting cracks, the general stress–strain relation can be expressed as (Lawn and Marshall, 1998)

$$\varepsilon = \frac{\sigma}{E_o} + \frac{dW}{d\sigma}. \tag{2}$$

Since the specimens were tested in compression, the cracks are likely to remain closed. The crack energy is given by the sum of the work done on each individual sliding crack, for all activated orientations β. The sliding displacement is proportional to the difference between the shearing force and friction for each β. By considering non-interacting cracks and a friction law given by (1), the crack energy for the unloading segment is given by (Lawn and Marshall, 1998)

$$W_{unloading}(\sigma) = \frac{\rho}{E_o} \int_0^{\arctan((\sigma_{max}-\sigma)/(\mu(\sigma_{max}+\sigma)))} (\sin\beta\cos\beta + \mu\sin^2\beta)\sin\beta\cos^2\beta \left(\frac{\sigma_{max}(\sin\beta\cos\beta - \mu\sin^2\beta)}{\sin\beta\cos\beta + \mu\sin^2\beta} - \sigma\right)^2 d\beta, \tag{3}$$
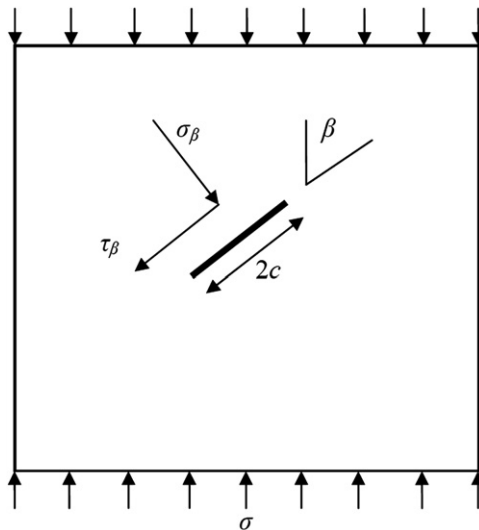

Fig. 12. Illustration of a closed crack in the material under uniaxial compression (after Lawn and Marshall, 1998).

where σ_{max} is the maximum stress attained prior to unloading, μ is the friction coefficient on the crack face and ρ is the crack configuration coefficient which contains information on the size, shape and density of the cracks, and is given by (Lawn and Marshall, 1998)

$$\rho = \Omega \eta n_v \overline{c^3}, \tag{4}$$

where n_v is the number of cracks by unit volume, c is the characteristic crack dimension to give a crack area of $A = \Omega c^2$, where Ω is a dimensionless constant, and η is a dimensionless crack geometry constant. The bar in the expression $\overline{c^3}$ denotes the average over all the cracks in the solid. For penny-shaped cracks considered here, $\Omega = \pi$, c is the crack radius and $\eta = 8(1-v)/3\pi$. It is important to note from Eq. (3) that during unloading, the range of β of activated cracks depends on the stress the material is bearing, thus not all the cracks begin to slide at the same time—cracks with small β have a smaller friction force and are more likely to start sliding before cracks with larger β do. Using the same approach, the crack energy for the reloading segment is given by (Lawn and Marshall, 1998)

$$W_{reloading}(\sigma) = \frac{\rho}{E_o} \int_0^{\arctan(1/\mu)} (\sin\beta\cos\beta - \mu\sin^2\beta)\sin\beta\cos^2\beta\sigma^2 d\beta. \tag{5}$$

Note that for the reloading segment, the range of angles β corresponding to sliding microcracks – defining the integration domain in both Eqs. (3) and (5) – is only a function of μ which, unlike the unloading segment, remains independent of the magnitude of σ and σ_{max}. As a result, one will obtain a linear relationship between stress and strain during the reloading phase, while cracks are sliding. By taking advantage of this property, we can now propose a rather simple procedure to measure the crack density from the shape of the reloading stress–strain curve.

4.1.3. Determination of the damage parameter $n_v\overline{c^3}$ from the reloading stress–strain curves

The damage parameter $n_v\overline{c^3}$ introduced in Eq. (4), is expected to depend on the maximum strain ε_{max} attained by the specimen in previous cycles. We will make here the assumption that the crack network configuration (density, shape, size, etc.) depends only on this parameter, and does not evolve as far as the applied strain remains inferior to ε_{max}. As a result, the proposed model does not describe how the cracks are being created but how the material behaves for a given crack configuration. We will use it as a way to extract ρ, using the shape of the reloading stress–strain curves, as explained here.

Following the previous discussion, the stress–strain response for the reloading segment with crack sliding is simply obtained by integrating Eq. (5) then substituting into Eq. (2)

$$\varepsilon = \frac{\sigma}{15E_0}\left(15 + 2\rho\left(\frac{2+3\mu^2+2\mu^4}{(1+\mu^2)^{3/2}} - 2\mu\right)\right). \tag{6}$$

Note that (6) gives a linear relationship between stress σ and strain ε, since for a given maximum strain ε_{max} attained in prior loadings, μ, ρ and E_o are constants. Thus, the effective modulus due to crack sliding E_{eff} is given by

$$E_{eff} = \frac{\sigma}{\varepsilon} = \frac{15E_o}{15 + 2\rho((2+3\mu^2+2\mu^4)/(1+\mu^2)^{3/2})(-2\mu))}. \tag{7}$$

Thus, the ratio between E_{eff} and E_o is given by

$$\frac{E_o}{E_{eff}} = 1 + \frac{2\rho}{15}\left(\frac{2+3\mu^2+2\mu^4}{(1+\mu^2)^{3/2}}\right). \tag{8}$$

Approximating the microcracks in the MAX ceramics by penny-shaped cracks, one can use Eq. (4) and express the damage parameter $n_v\overline{c^3}$ as a function of the ratio E_o/E_{eff}

$$n_v\overline{c^3} = \frac{45}{16(1-v)}\frac{(1+\mu^2)^{3/2}}{2+3\mu^2+2\mu^4}\left(\frac{E_o}{E_{eff}} - 1\right). \tag{9}$$

In the following, we will use this expression to characterize the development of the damage in the ceramics as a function of the applied strain: for each cycle with maximum applied strain ε_{max}, the measurement of the ratio E_o/E_{eff} in the reloading curve will be used with Eq. (9) to obtain the dimensionless parameter $n_v\overline{c^3}$. This ratio is obtained from the experiments by taking the average slope of the first segment of the reloading curve over that of the second segment. The presence of two stages during the reloading phase corresponding to a linear response without crack sliding followed by another linear response with different slope accompanied by crack sliding is clear on the experimental curves, as illustrated in Fig. 13. This figure summarizes also the predictions of the models and the proposed interpretation of the different regimes of the reloading–unloading cycle.

The ratio E_o/E_{eff} is represented as a function of ε_{max} in Fig. 14 and is found to vary linearly with the applied maximal strain. The slope E_{eff} of the second segment is determined by the tangent modulus of the segment of the curve closer to the maximum stress achieved from prior loadings. The dotted line in Fig. 14 shows the best linear fit for the experimental data

$$\frac{E_o}{E_{eff}} = 103\varepsilon_{max} + 0.907. \tag{10}$$
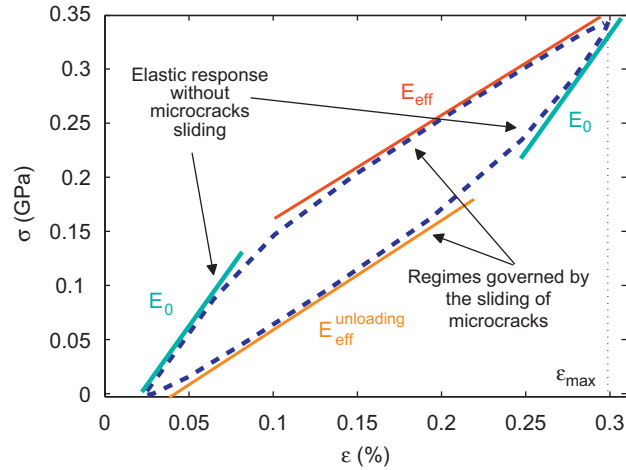
Fig. 13. The various regimes characterizing the experimental reloading–unloading cycles and their interpretation within the micromechanical model. The doted curve corresponds to the experimental response of a porous Ti$_2$AlC specimen to a reloading–unloading cycle with $\varepsilon_{max}=0.30\%$.
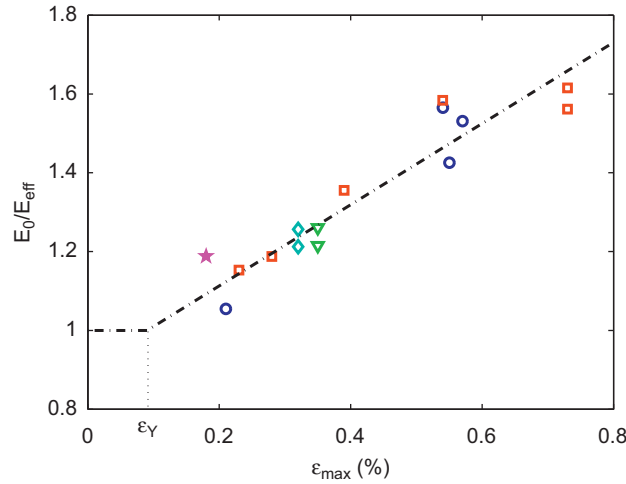
Fig. 14. Ratio E_o/E_{eff} versus ε_{max} attained during each loading cycle for dense Ti$_2$AlC (symbols represent different specimens). Let us note that in the range $0 < \varepsilon_{max} < \varepsilon_Y \approx 0.1\%$, the specimens behave linearly and reversibly so $E_0=E_{eff}$.

Let us note that this relationship does not hold for small values of ε_{max}. Indeed, for $\varepsilon_{max} < \varepsilon_y=0.18\%$, experimental stress–strain data show linear elastic behavior, so E_{eff} is equal to E_o for this range of applied strains.

Using the theoretical prediction of Eq. (9), one can now obtain the damage parameter $n_v\overline{c^3}$ at different levels of applied strain. In Eq. (9), $n_v\overline{c^3}$ is expressed as a function of the ratio E_o/E_{eff} and the parameters μ and v. The friction coefficient μ is expected to be independent of ε_{max} and we will first assume $\mu=0.1$. This choice will be discussed subsequently when we will reconstruct the stress–strain curve in the unloading phase and will compare it with the experimental data. As shown in Fig. 7, Poison's ratio v varies only weakly with the applied strain—from 0.20 to 0.18 in the range investigated. As a result, the parameter $1/(1-v)$ changes by less than 2% between both values, and we take a constant Poisson's ratio with $v=0.20$, corresponding to its value before any loading. Combining Eqs. (9) and (10), one obtains the dimensionless quantity $n_v\overline{c^3}$ characterizing the geometrical properties of the damage in the MAX ceramics as a function of the applied strain

$$n_v\overline{c^3}(\varepsilon_{max}) = 201\varepsilon_{max}-0.182. \tag{11}$$

This relationship will be compared in the subsequent section with direct measurements of the crack density and crack size made on the actual specimens loaded to different ε_{max}, and obtained from the analysis of SEM images of their microstructure.

The damage parameter $n_v\overline{c^3}$ is found to be relatively large for specimens tested up to high level of strain. For example, at $\varepsilon_{max}=0.75\%$ corresponding to about half of the failure strain, $\overline{c^3}/\overline{v}$ is found to be as large as 1.3. The question remains whether

the assumption of non-interacting cracks is valid at such densities. Approximate schemes, such as self-consistent scheme (SCS) (Budiansky and O'Connell, 1976) and differential scheme (DS) (Hashin, 1988) were developed to capture the effects of crack interactions. However, these schemes always assume that crack interactions result in stress-amplifying configurations, which Kachanov (1992) has proven that may not always be the case. Using numerical simulations, Kachanov generated randomly oriented and parallel cracks with varying crack densities (up to $n_v \overline{c^3} = 0.35$) in different 2D specimens. The crack interactions were then considered using stress superposition at each crack. He found that both SCS and DS misrepresent the actual crack interactions and that the non-interacting scheme provides the most accurate description up to the largest crack density ($n_v \overline{c^3} = 0.35$) that was tested. Kachanov concluded that the non-interacting cracks scheme remains accurate for larger values of crack density than expected because of the negating effect of stress shielding effect which is overlooked in both the SCS and DS schemes. Liu and Nakamura (2008) investigated the role of crack interaction by comparing the theoretical predictions of models neglecting this effect with finite element calculations for very large crack densities (up to density of the order of one), and found surprisingly good agreement between both approaches.

In the case of Ti$_2$AlC, a significant part of the relevant range of $n_v \overline{c^3}$ is larger than 0.35 and even beyond 1 for the largest value of applied strain. The cracks usually occur between the laminates of each grain (see Figs. 9 and 19), creating parallel cracks within each grain, but randomly oriented cracks within the material itself since the grains are randomly oriented. Kachanov (1992) demonstrated that the stress shielding interaction is more pronounced in parallel cracks arrays, and that crack interactions are found to be much weaker in 3D specimens (Kachanov and Laures, 1989). Therefore, while the specific case of $n_v \overline{c^3} > 0.35$ remains to be studied, it is felt that the non-interacting crack scheme can be used confidently as a first step in developing a model.

4.1.4. Construction of the unloading stress–strain curves

The crack characteristic coefficient ρ and friction coefficient μ are constant during unloading. Thus the unloading stress–strain relationship with crack sliding can be obtained by first integrating Eq. (3) numerically for various values of $\sigma < \sigma_{max}$ and then substituting the crack energy into Eq. (2) to obtain the stress–strain relationship. We use here the value of ρ obtained from the stress–strain response in the reloading part of the cycle. The tangent modulus of the resulting stress–strain curve is then determined by numerical differentiation and compared with the experimental results as shown in Fig. 15 for two different maximal strain levels.

It is observed that the model is able to predict E_t rather accurately for these two values, i.e. ε_{max}=0.55% and 0.71%. Eqs. (2) and (3) define the stress–strain relationship beyond the onset of crack sliding, corresponding to the segment of the unloading curve with the smallest value of E_t. In the model, the initial slope in the unloading phase corresponds to E_o (before the initiation of crack sliding) and is provided by the analysis of the reloading phase for small applied strain, before the cracks start to slide. As a consequence, the location for onset of sliding, marked by the discontinuity of E_t in Fig. 14, is obtained by the intersection between the elastic unloading curve ($E_t=E_o$) starting from (ε_{max}, σ_{max}), and the curve obtained using (2) and (3) (to describe the stress–strain behavior with crack sliding) starting from (ε_{res}, 0). This location cannot be identified by our model and the residual strain ε_{res} has been taken equal to its experimental value.

The full stress–strain behavior is shown in Fig. 16. The figure shows that the predicted stress–strain relationship agrees well with the experimentally measured curve. The reloading curve is the same whatever the value of μ is, since the reloading curve was used to obtain ρ by solving (10) and (11). Hence, a different choice of μ will simply result in a different value for ρ, but does not change the resulting stress–strain curve during reloading. The shape of the unloading curve however, is dependent on the value of μ. In particular, the position of the crossover between the regime with crack sliding and no sliding strongly depends on the choice of μ as shown in Fig. 16. As a result, it can be used as a means to determine the appropriate value for the friction coefficient. Fig. 17 shows the values of μ that minimize the difference between the theoretical and experimental unloading stress–strain curves for specimens loaded to various ε_{max}. The friction coefficient μ is found to be independent on ε_{max}, as expected. Fig. 17 validates a posteriori our initial choice μ=0.1 used to extract the crack density from the reloading curve. This value is consistent with the low value of μ reported in other MAX phases (Barsoum and El-Raghy, 2001).

Finally, we checked the stress–strain predictions of the model on other experimental results for specimens tested to various ε_{max} as well, as exemplified in Fig. 18. It is again observed that the predicted and measured behavior of Ti$_2$AlC agree quite well.

On the very same figure, we have analyzed the effect of a more complex friction law on the overall mechanical behavior of the specimens, as proposed e.g. by Lawn and Marshall (1998). Introducing a cohesive stress τ_c between the opposite faces of microcracks, the friction law used in our model in Eq. (1) becomes $\tau_f = \tau_c + \mu\sigma\sin^2\beta$. Taking the value $\tau_c = 45$ MPa,[1] one obtains the dot curve represented in Fig. 18 that one can compare with the predictions obtained taking τ_c=0. Since both curves are quite close in both the loading and unloading part of the stress strain curve, the value of τ_c does not influence the crack density extracted from it. As a result, we considered only a friction law of the type given in Eq. (1) taking τ_c=0. This has two important consequences: (i) the use of such a simplified friction law results in an explicit relationship between the crack density and the ratio of effective Young's modulus observed in the reloading phase (see Eq. (8)). This represents the basis for the simple procedure proposed here to characterize damage spreading within MAX

---

[1] This value has been determined by comparing predictions of the model using the friction law with non-zero cohesive stress with the experimental data. In particular, with μ=0.1, it leads to a the value σ_c=0.2 GPa for the onset of crack sliding in the reloading phase, as observed experimentally.
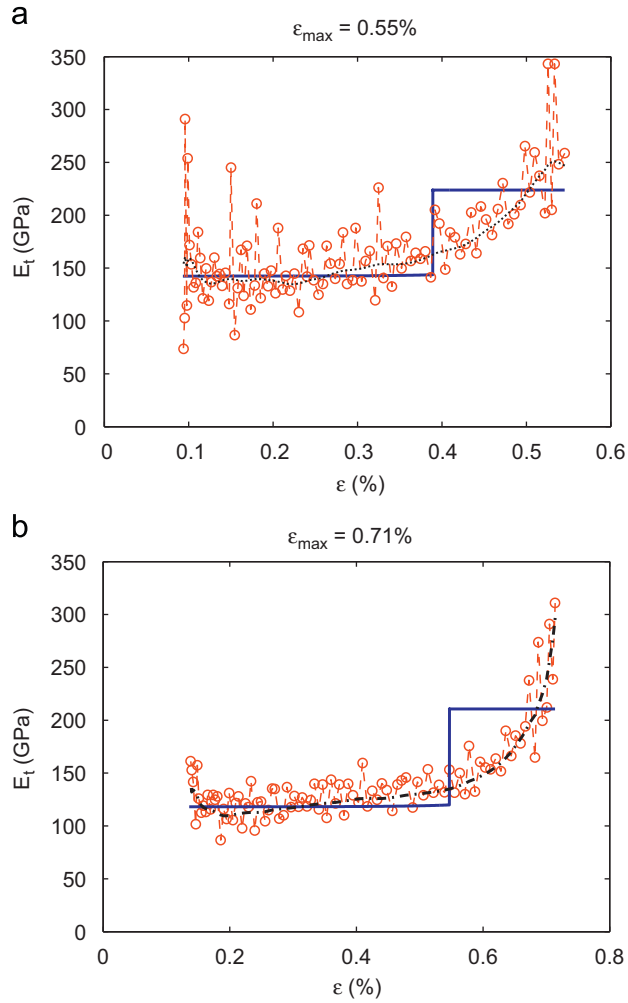
Fig. 15. Comparison between predicted (solid) and experimental (dot) tangent modulus E_t for the unloading curves for two specimens loaded to different maximum strains ε_{max}. The experimental results correspond to the smoothed signal of the raw variations in red of the tangent modulus. (For interpretation of the references to color in this figure legend, the reader is referred to the web version of this article.)
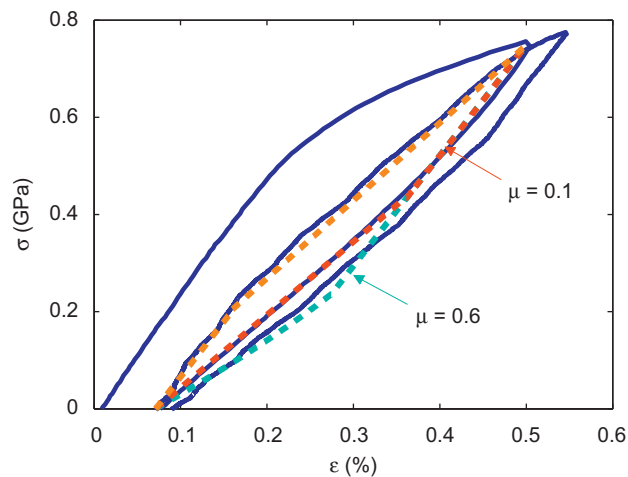
Fig. 16. Effect of μ on the unloading curve (dashed lines—model, solid lines—experiment).
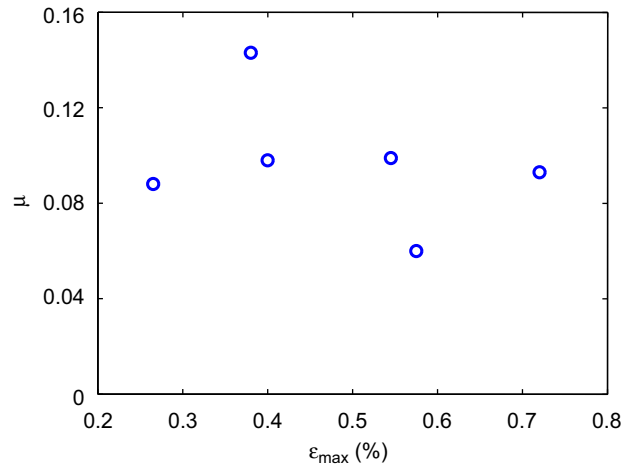
Fig. 17. Values for μ that minimize the difference between the theoretical and experimental unloading stress–strain curves for specimens tested to different ε_{max}. Note the average value of $\mu = 0.1$.
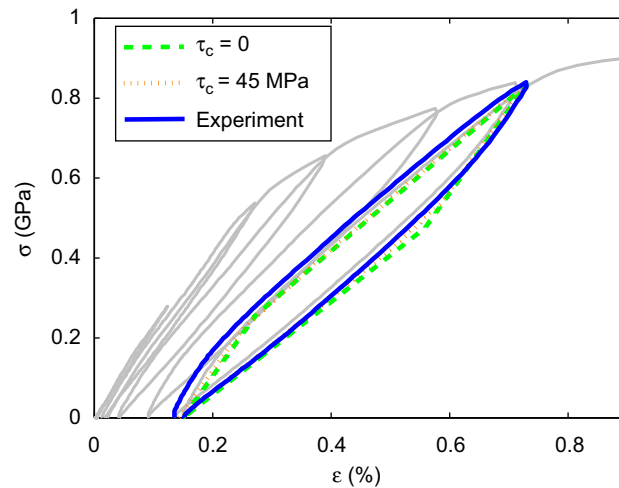
Fig. 18. Comparison of the predicted and experimentally measured stress–strain curves (dashed lines—model, solid lines—experiment).

ceramics from their stress–strain behavior; (ii) the reloading part is piecewise linear and has been constructed the following way: an initial linear segment with slope E_0 is plotted until $\sigma = \sigma_c$ corresponding to the onset of crack sliding—we found $\sigma_c = 0.2$ GPa from the experimental stress–strain curves.[2] A second linear segment with slope E_{eff} as measured from the experimental stress–strain reloading curve (see Section 4.1.3) is then plotted.

Finally, let us note that a microcracks friction based model was also recently successfully applied to interpret experimental measurements, here in the context of thermally sprayed ceramics coating (Liu and Nakamura, 2008). As in the present study, comparison between theoretical predictions and experimental data provided interesting insights on the evolution of the material microstructure and damage with the external loading conditions.

4.2. Validation of the model: measurement of crack density using SEM images

In the previous section, the mechanical behavior of Ti$_2$AlC has been interpreted using a micromechanics model where the friction between the two opposite surfaces of cracks is responsible for the energy dissipation and the hysteresis loops observed

---

[2] In strict accordance to the model with $\tau_c = 0$, there should be no initial elastic segment in the reloading regime—crack sliding occurs immediately at the very onset of loading. However, to account for the experimental observations, such a regime is introduced artificially for $0 < \sigma < \sigma_c = 0.2$ GPa. The choice of $\tau_c = 0$ in our theoretical description is justified by the observation that the cohesive stress has a negligible influence on the theoretical stress–strain curve. In particular, the extracted crack density from the stress–strain curve is not affected by the choice of τ_c.
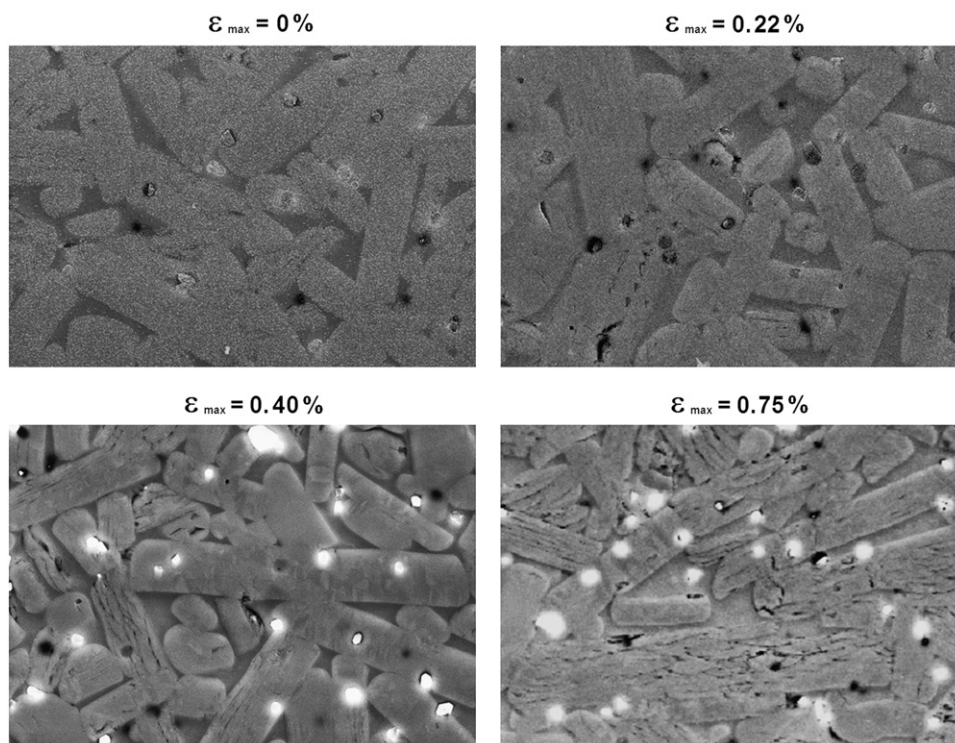
Fig. 19. SEM images $60 \times 43\ \mu m^2$ of the microstructure of dense Ti$_2$AlC at different strain levels. Note both inter-granular and delamination cracks.

for this material under cyclic loading. In this approach, the width of the hysteresis loops is directly related to the density of cracks through the parameter $n_v\overline{c^3}$ that characterizes the geometry of the damage in the material. As a result it was possible to deduce this parameter from the shape of the stress–strain curves. In this section, the crack density obtained from the stress–strain measurements are now compared directly with the measured crack density from the SEM images.

Typical images $60 \times 43\ \mu m^2$, corresponding to four different maximum applied strains are shown in Fig. 19. Their corresponding stress–strain response during the compression is shown in Fig. 6. Cracks can be clearly identified on the images. Many of them have propagated from a grain boundary to another, remaining confined to a single grain. It is also interesting to note that they are almost all oriented along the largest (longitudinal) dimension of the anisotropic grains, suggesting delamination between the weak planes (transverse) of the Ti$_2$AlC single crystals.

From Fig. 19, a qualitative estimation of the geometry of the crack network at different strain levels suggests that the damage is more extensive at larger strains. To study more quantitatively the damage accumulation, a procedure has been developed whose result is shown in Fig. 20, taking as an example the SEM image presented in Fig. 19 with ε_{max}=0.40%. Here, the position and orientation of the cracks were first identified manually. It was not possible to perform this process using an automated procedure because of the presence of the grain boundaries that could be misinterpreted as cracks. Therefore, this task was first performed reproducing the crack network on a semitransparent paper, followed by digitizing the drawing (see the left panel of Fig. 20). The geometry of the damage and its density were then analyzed defining the surrounding area of each individual crack, as represented on the right part of Fig. 20. This was done by applying a Voronoi tessellation based algorithm on the crack network. This procedure enables a precise measurement of the properties of the crack network, because it is possible to exclude the crack – and their surrounding area – close to the edges of the image, and for which full crack length and its environment are partly unknown. The selected cracks, sufficiently far away from the edges, are represented in dotted lines in Fig. 20.

With the above described procedure, it is now possible to measure precisely the typical area $\langle S \rangle$ surrounding a single crack on the images. Selecting only the cracks sufficiently far from the edges, one can get an unbiased estimate of the number of cracks n_s=1/$\langle S \rangle$ per unit surface. The variation of the crack density by unit surface with the maximum applied strain is represented on the left hand side of Fig. 21. As observed qualitatively in Fig. 19, the crack density increases with the loading. The error bars are defined from the variations of densities obtained from one image to another (at least two sets of two images of size 60×40 and $30 \times 20\ \mu m^2$ were analyzed for each strain level). Note that such a quantity defined on the SEM images is related to but different from the effective crack density in the ceramics corresponding to the number of cracks by unit volume. Their relation is provided later in Appendix. The average half-length $\overline{c}_s$ of cracks, as measured on the SEM images, is then computed for each strain level. This typical crack length is found to remain almost constant with the external loading, as shown on the right hand side of Fig. 21.
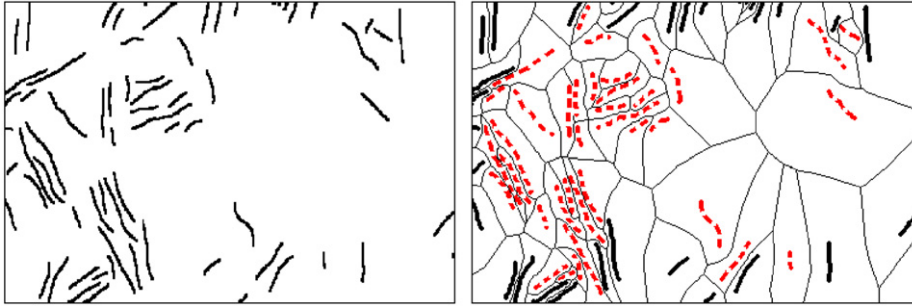
Fig. 20. Left: crack network as observed on the $60 \times 43 \, \mu m^2$ SEM image corresponding to $\varepsilon_{max} = 0.4\%$, i.e. the bottom right SEM image of Fig. 18. Right: the corresponding Voronoi diagram of the cracks that defines the surrounding surfaces. Only the cracks represented by dotted lines, sufficiently far from the side of the image, are considered in the calculation. (In order to compute the number n_s of cracks by unit surface, the ones close to the side of the images are excluded from the calculation. As a result, $n_s = 1/\langle S \rangle = N_{crack}/S_{crack}$ where N_{crack} is the number of cracks on the image after exclusion, and S_{crack} is the total area surrounding these cracks, as defined by the Voronoi tessellation (see Fig. 19). Without such a procedure, S_{crack} would be underestimated (since some part of the surface surrounding the excluded crack is outside of the image), and so n_s would be overestimated).
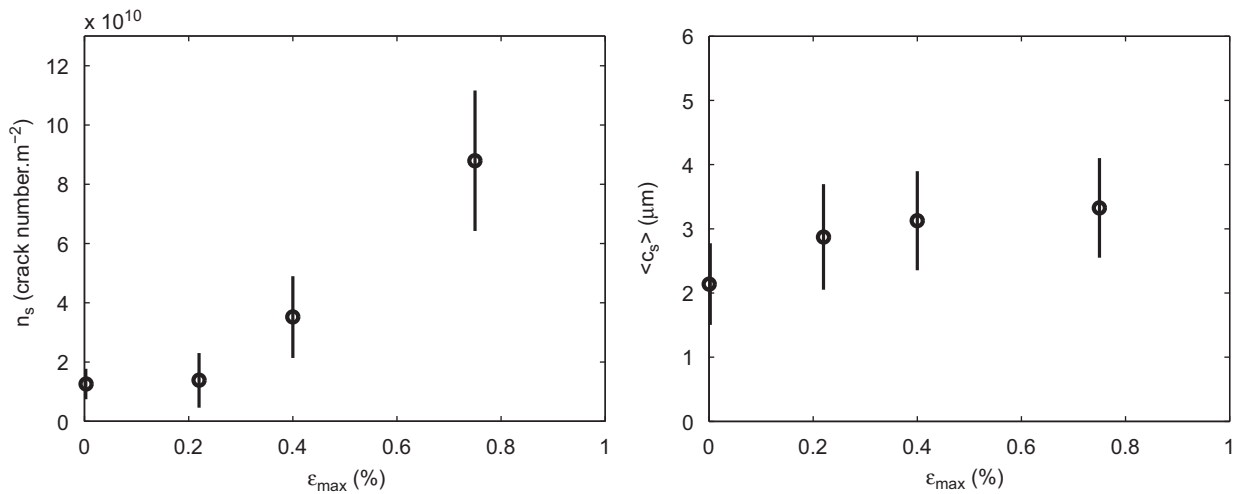

Fig. 21. Variations of the number of cracks n_s by unit surface and the mean crack length $\overline{c}_s$ observed on the SEM images with respect to the applied maximum strain.

Strictly speaking, the damage parameter involved in the theoretical description of the MAX ceramics is defined from the product of $\overline{c^3}$ – the average of the cube of the crack length – with the number of cracks n_v by unit volume. Obtaining these quantities from SEM images – two dimensional cut of the 3D crack network – is not straightforward. Using stereological relationships detailed in Appendix, one can however relate our 2D observations presented in Fig. 20 with the damage parameter as defined in the micromechanics model:

$$n_v \overline{c^3} \approx 1.36 n_s \overline{c}_s^2. \tag{12}$$

This quantity is then computed on each image, and after averaging over those corresponding to a same level of strain, one obtains its variations with ε_{max} as presented in Fig. 22. Error bars are computed from the fluctuations from one image to another. The comparison with the value obtained from the analysis of the hysteresis loops of the samples under cyclic loading using the micromechanics model presented in Section 4.1.4 is also shown on the same figure. The agreement with the analytically predicted value is good over the full range of strain investigated.

The results shown in Fig. 22 can be viewed as a validation of the proposed model, including the underlying assumptions, such as non-interacting and randomly oriented cracks (Section 4.1.4) for Ti$_2$AlC. It is important to note that the crack density is the only relevant adjustable parameter of the model since the value of μ has been deduced directly from the stress–strain curve. The present results suggest that sliding of cracks, whose density increases with the maximum applied strain, is the main dissipative mechanism which gives rise to the hysteresis loops observed for Ti$_2$AlC. This differs from the interpretation proposed by Barsoum et al. (2003) where a dislocation based mechanism was invoked to explain the hysteretic response. The dislocation-based mechanism was postulated, with emphasis on the value of the dissipated energy without looking into detail at the stress–strain relationship during both loading and unloading. In addition, no direct observation of such a reversible microscopic mechanism was reported. The present work used a single
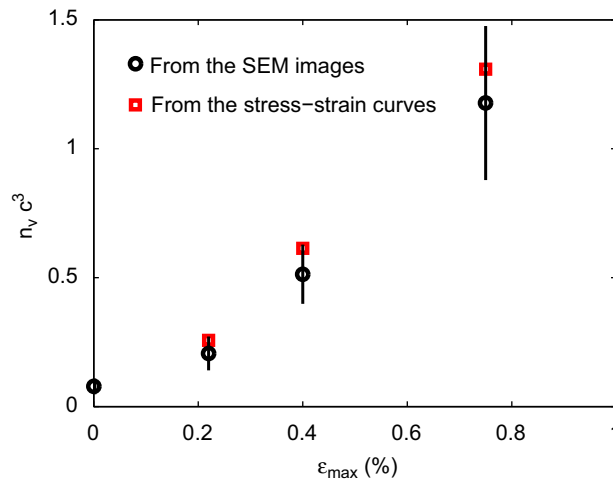
Fig. 22. Variations of the damage parameter $n_v \overline{c^3}$ with the applied strain as measured from the SEM images and from the mechanical behavior of dense Ti$_2$AlC.

micromechanical model based on measurable parameters (stress, strain) and one dominant dissipation mechanism, friction between faces of microcracks that are evidenced on SEM images of the Ti$_2$AlC microstructure. It accurately reproduces the stress–strain behavior during loading and unloading (thus predicting the correct dissipated energy), while providing an accurate estimation of the crack density at every stage of the loading. As such, the present results and their micromechanical interpretation are not only restricted to the MAX phases, but can be applied to other classes of quasi-brittle materials for which microcracking is an important failure mechanism.

5. Conclusions

The mechanical behavior of Ti$_2$AlC, a MAX phase material, was examined and modeled. The hysteretic stress–strain behavior during unloading–reloading cycles (a unique characteristic of the MAX phases) was observed for Ti$_2$AlC as well. It was observed through careful experimentation that this material behaves like a linearly elastic solid before its yield point, beyond which, its stress–strain behavior (for monotonic loading) resembles a power-law relationship and hysteresis loops can be observed during the unloading and reloading cycles.

The specimens, both fractured and intact, were examined using the SEM. Damage mechanisms such as delamination and inter-granular cracks and kink bands were observed. Based on these mechanisms, a damage model was proposed to describe the mechanical behavior observed in the uniaxial experiments. This model considered the damage accumulation to be a function of the maximum strain attained by the material. The kink bands likely reduced the elastic modulus of the material while the sliding of the cracks likely resulted in the hysteretic unloading–reloading stress–strain behavior.

The micromechanical model for crack sliding used to describe the unloading and reloading of Ti$_2$AlC is based on the model proposed by Lawn and Marshall (1998). Assuming Coulomb frictional law between the crack faces, it was demonstrated that the crack density can be easily determined using the ratio between the elastic modulus and the 'sliding modulus' (slope of the stress–strain curve corresponding to crack sliding) of the reloading curve, while the frictional coefficient can be obtained using the corresponding unloading curve. The model was found to be able to describe the stress–strain behavior of Ti$_2$AlC. In addition, SEM images for four specimens loaded to various maximum strains were analyzed to obtain the quantitative measure for the crack density. The predicted and measured crack densities at each maximum strain attained by the material were compared and found to be in reasonably good quantitative agreement.

To conclude:

- Experimental results show evidence of crack accumulation in Ti$_2$AlC when loaded beyond its yield point.
- The micromechanical model used to describe the stress–strain behavior relies only on two "unknown" parameters, the crack density and friction coefficient.
- The crack density can be determined from the ratio between the elastic and sliding modulus.
- The friction coefficient can be computed using the unloading stress–strain curves.
- The predicted crack density using this model was found to be in good agreement with that measured quantitatively using statistical analysis of the SEM images.
- The good agreement between the experimental results and model predictions suggests that the main dissipative mechanism responsible for the hysteretic unloading reloading curves, is friction between the microcrack faces in the material.
- This model can be used as a simple technique to obtain crack densities and friction coefficient in other brittle or quasi-brittle materials with microcracks as well.

Acknowledgments

Appendix. Stereological model: computing the 3D damage parameter $n_v \overline{c^3}$ from 2D SEM images

As a test of the micromechanical model proposed to account for the hysteretic behavior of Ti_2AlC ceramics under cyclic loading, the damage parameter $n_v \overline{c^3}$ predicted theoretically from the mechanical response of the ceramic is compared with the values obtained from a direct observation of the ceramic microstructure (see Fig. 22). The information on the crack network as obtained experimentally being limited to SEM images that correspond to 2D cut of the 3D crack network, one needs first to relate the quantity $n_v \overline{c^3}$ involved in the micromechanics model to quantities directly measurable on the images, such as the density n_s of cracks by unit surface and the average crack length $\overline{c}_s$ observed on SEM images.

As a starting point, we use the classical relation of stereology that relates the total crack length by unit surface L_A (in $\mu m/\mu m^2$) to its total area by unit volume S_v (in $\mu m^2/\mu m^3$) (Russ and Dehoff, 2000; Nemati and Stroeven, 2001)

$$S_v = \frac{4}{\pi} L_A. \tag{A.1}$$

L_A can be measured on the SEM images and is related to the average crack half-length and the crack density, both given in Fig. 21 as a function of ε_{max}, by $L_A = 2 n_s \overline{c}_s$. The same kind of relation holds for S_v leading to $S_v = \pi n_v \overline{c^2}$ where n_v is the number of cracks by unit volume and c is the radius of the cracks, assumed to have a penny shape as also assumed in the micromechanics model.

It is now possible to express $\overline{c^2}$ as a function of these quantities as

$$\overline{c^2} = \frac{8}{\pi^2} \frac{\overline{c}_s n_s}{n_v}. \tag{A.2}$$

To obtain an expression for $\overline{c^3}$, it is necessary to make an assumption on the distribution of crack sizes. Assuming a Gaussian distribution of normalized standard deviation $\sigma_n = (\sqrt{\overline{c^2} - \overline{c}^2}/c)$, the average of c, c^2 and c^3 are related by

$$\overline{c^3} = 3\overline{c^2} - 2\overline{c}^3. \tag{A.3}$$

Expressions that relate $\overline{c}$ and n_v to quantities measured on the SEM images are still lacking. These are provided by

$$\overline{c} = \alpha_0 \overline{c}_s, \tag{A.4}$$

$$n_v = \beta_0 \frac{n_s}{\overline{c}_s}, \tag{A.5}$$

where α_0 and β_0 are constants depending on σ_n only. Using Eqs. (A.2)–(A.4) with the definition of σ_n allows to relate β_0 to α_0

$$\alpha_0 \beta_0 = \frac{8}{\pi^2 (1 + \sigma_n^2)}. \tag{A.6}$$

It is now possible to express the damage parameter $n_v \overline{c^3}$ as a function of quantities one can measure on the SEM images, using successively Eq. (A.3), (A.2) and (A.4), and finally Eqs. (A.5) and (A.6):

$$\frac{\overline{c^3}}{\nu} = \frac{24}{\pi^2} \alpha_0 n_s \overline{c}_s^2 \left[1 - \frac{2}{3(1 + \sigma_n^2)} \right]. \tag{A.7}$$

The constant α_0 is measured numerically by simulating a network of penny-shaped cracks distributed in a Gaussian distribution with standard deviation σ_n and computing the properties of images obtained from cuts of the 3D networks, and after averaging over a large number of configurations. α_0 is found to decrease slightly with σ_n, taking the value 1.678 for a homogeneous distribution of cracks, corresponding to $\sigma_n = 0$. As the term in bracket in expression (A.7) of the damage parameter increases faster with σ_n, the overall behavior of the ratio $n_v \overline{c^3}$ corresponds to an increase with the standard deviation of the crack size distribution, as expected from its numerator. However, this increase is small, e.g. of the order of 10% for $\sigma_n = 0.5$ with respect to $\sigma_n = 0$. As a result, we will neglect here the effect of σ_n on the value of the damage parameter, and will take $\alpha_0(\sigma_n = 0) = 1.678$ and $\sigma_n = 0$ in Eq. (A.7). This provides Eq. (12) used in Section 4 to compute the damage parameter $n_v \overline{c^3}$ involved in our micromechanics model from the geometrical properties of the crack network as measured on the SEM images.

References

Barsoum, M.W., El-Raghy, T., 2001. The MAX phases: unique new carbide and nitride materials. Am. Sci. 89, 334–343.
Barsoum, M.W., Ali, M., El-Raghy, T., 2000. Processing and characterization of Ti_2AlC, Ti_2AlN, and $Ti_2AlC_{0.5}N_{0.5}$. Metall. Mater. Trans. A 31, 1857–1865.

Barsoum, M.W., Brodkin, D., El-Raghy, T., 1997. Layered machinable ceramics for high temperature applications. Scr. Mater. 36, 535–541.
Barsoum, M.W., Salama, L., El-Raghy, T., 2002. Thermal and electrical properties of Nb_2AlC, $(Ti, Nb)_{(2)}AlC$ and Ti_2AlC. Metall. Mater. Trans. A 33, 2775–2779.
Barsoum, M.W., Zhen, T., Kalidindi, S.R., Radovic, M., Murugaiah, A., 2003. Fully reversible, dislocation-based compressive deformation of Ti_3SiC_2 to 1 GPa. Nat. Mater. 2, 107–111.
Barsoum, M.W., Zhen, T., Zhou, A., Basu, S., Kalidindi, S.R., 2005. Microscale modeling of kinking nonlinear elastic solids. Phys. Rev. B 71, 134101.
Budiansky, B., O'Connell, R.J., 1976. Elastic-moduli of a cracked solid. Int. J. Solids Struct. 12, 81–97.
Frank, F.C., Stroh, A.N., 1952. On the theory of kinking. Proc. Phys. Soc. London Sec. B 65, 811–821.
Hashin, Z., 1988. The differential scheme and its application to cracked materials. J. Mech. Phys. Solids 36, 719–734.
Kachanov, M., 1982. A microcrack model of rock inelasticity—part I: frictional sliding on microcracks. Mech. Mater. 1, 19–27.
Kachanov, M., 1992. Effective elastic properties of cracked solids: critical review of some basic concepts. Appl. Mech. Rev. 45, 304–335.
Kachanov, M., Laures, J., 1989. 3-Dimensional problems of strongly interacting arbitrary located penny-shaped cracks. Int. J. Fract. 41, 289–313.
Kalidindi, S.R., Zhen, T., Barsoum, M.W., 2006. Macroscale constitutive modeling of kinking nonlinear elastic solids. Mater. Sci. Eng. A 418, 95–98.
Lawn, B.R., Marshall, D.B., 1998. Nonlinear stress–strain curves for solids containing closed cracks with friction. J. Mech. Phys. Solids 46, 85–113.
Lehner, F.K., Kachanov, M., 1995. On the stress–strain relations for cracked elastic materials in compression. In: Rossmanith, H.P. (Ed.), Proceedings of the Second International Conference on the Mechanics of Jointed and Faulted Rock, Vienna, Austria.
Liu, Y., Nakamura, T., 2008. Anelastic behavior of plasma-sprayed zirconia coatings. J. Am. Ceram. Soc. 91, 4036–4043.
Nemati, K.N., Stroeven, P., 2001. Strereological analysis of micromechanical behavior of concrete. Mater. Struct. 34, 486–494.
Russ, J.C., Dehoff, R.T., 2000. In: Practical Strereology. Kluwer Academic Publishers, New York.
Sun, Z.M., Murugaiah, A., Zhen, T., Zhou, A., Barsoum, M.W., 2005. Microstructure and mechanical properties of porous Ti_3SiC_2. Acta Mater. 53, 4359–4366.
Walsh, J.B., 1965. The effect of cracks on the uniaxial elastic compression of rocks. J. Geophys. Res. 70, 399–411.
Wang, X.H., Zhou, Y.C., 2003. High-temperature oxidation behavior of Ti_2AlC in air. Oxid. Met. 59, 303–320.
Zhen, T., Barsoum, M.W., Kalidindi, S.R., 2005. Compressive creep of fine and coarse-grained T_3SiC_2 in air in the 1100–1300 °C temperature range. Acta Mater. 53, 4163–4171.
Zhou, A.G., Barsoum, M.W., Basu, S., Kalidindi, S.R., El-Raghy, T., 2006. Mechanical damping in porous Ti_3SiC_2. Acta Mater. 54, 1631–1639.